Multibit memory operation of metal-oxide bi-layer memristors

Spyros Stathopoulos[1], Ali Khiat[1], Maria Trapatseli[1], Simone Cortese[1], Alexantrou Serb[1], Ilia Valov[2] and Themis Prodromakis[1*]

[1]Department of Electronics and Computer Science, Faculty of Physical Science and Engineering, University of Southampton, University Road, SO17 1BJ, Southampton, United Kingdom.

[2]Forschungszentrum Jülich, Wilhelm-Johnen-Straße, 52428, Jülich, Germany

*Corresponding Author: Themis Prodromakis (Email: t.prodromakis@soton.ac.uk)

Emerging nanoionic memristive devices are considered as the memory technology of the future and have been winning a great deal of attention due to their ability to perform fast and at the expense of low-power and -space requirements. Their full potential is envisioned that can be fulfilled through their capacity to store multiple memory states per cell, which however has been constrained so far by issues affecting the long-term stability of independent states. Here, we introduce and evaluate a multitude of metal-oxide bi-layers and demonstrate the benefits from increased memory stability via multibit memory operation. We propose a programming methodology that allows for operating metal-oxide memristive devices as multibit memory elements with highly packed yet clearly discernible memory states. These states were found to correlate with the transport properties of the introduced barrier layers. We are demonstrating memory cells with up to 6.5 bits of information storage as well as excellent retention and power consumption performance. This paves the way for neuromorphic and non-volatile memory applications.

Resistive memory devices, also known as memristors[1], are nowadays attracting considerable attention due to the breadth of potential applications ranging from non-volatile memory[2] to neuromorphic systems[3,4] and reconfigurable circuits[5]. Their competitive advantage over established complementary metal-oxide-semiconductor (CMOS)-based memory stems from their capability to support a multitude of states, long retention characteristics, fast switching and ultra-low power consumption[6]. Many technologies have been put forward as potential winners of the non-volatile memory race[7], namely phase-change (PCRAM)[8], magnetic (MRAM)[9] and resistive random access memory (ReRAM)[10]. Although MRAM and PCRAM are considered more reliable, they are constraint by power and/or scalability issues[11,12]. In contrast, ReRAM has shown capacity of operating in the femtojoule regime[13], with functional devices reported at feature sizes that outperform CMOS[14,15]. However, even though the realisation of bistable memory devices (1-bit) is apparent from the very nature of the memristor to variate between two resistive states[16] the implementation of a device that can reliably be programmed at a multitude of distinct resistive states still poses a significant challenge. Although there are some recent reports of multibit capable metal-oxide memory cells[17], most works in literature are limited to no more than 3 bits.[18–22]

Resistive switching has been observed in many metal-oxide systems[23], with Ta_2O_5[24,25], HfO_2[26] and TiO_2[27,28] being among the most popular. In all cases, the origin of switching has been attributed to either the drift of oxygen vacancies[28] and/or interstitials[29] or the formation of conductive filaments[30] within an active metal-oxide core under the influence of an applied electrical field. Within that context several studies have reported on the importance of interface interactions and properties[31], showing that the introduction of a thin interfacial barrier layer between the active layer and one of the electrodes can influence the electrochemical processes, the devices' stability[32,33], improve its switching characteristics and reduce the overall power consumption[34–37].

Taking into advantage these observations, we developed a series of 2-terminal prototype metal-insulator-metal (MIM) ReRAM cells, as depicted in Figures 1a, 1b and 1c, with bilayer structure using TiO_2 as solid electrolyte and seven different interface barrier layer configurations; all employing Pt top and bottom electrodes. The active layers studied were: 1) TiO_2-only, 2) Al_xO_y/TiO_2, 3) Ta_xO_y/TiO_2, 4) SiO_2/TiO_2, 5) ZnO/TiO_2, 6) HfO_x/TiO_2 and 7) WO_x/TiO_2. For all fabricated devices the thickness was maintained to 4 nm and 40 nm for the barrier and TiO_2 layer respectively. The size of the devices used in this paper is 20×20 μm^2. The TiO_2 layer is amorphous and stoichiometric as more details can be found in our previous[38,39]. Smaller and larger area devices, namely 10×10 μm^2 and 20×20 μm^2, were considered but no apparent impact on the multibit performance was observed. All prototypes were electroformed with 1 μs pulses of negative polarity ranging from -3 to -12 V in steps of 100 mV, to an operational resistive state range, typically between 20–150 kΩ, depending on the stack configuration (see supplementary fig. S1). Figures 1d and 1e illustrate the difference in resistive programming stability between the TiO_2-only and Al_xO_y/TiO_2 ReRAM cells. In both cases, 100 ns pulse ramps of alternating polarity from 1 to 2 V with 200 mV step are used as input stimulus. Considerable drift in programming can be observed in Figure 1d for the TiO_2-only devices, which practically results into non-discernible memory states even after 20 switching cycles. Although the stability of TiO_2-only devices can be further optimised at the expense of programing energy (see supplementary Figure S2), the comparable Al_xO_y/TiO_2 cells indicate a more stable behaviour, as observed in Figure 1e, overall maintaining a constant OFF/ON resistive ratio throughout the experiment. The more clear definition of low and high resistive states is similar to what Yu *et al* have reported for the HfO_x/AlO_x system[34] in comparison to the respective single layer cell.

The need for stable and reliable switching at minute resistive increments becomes increasingly important if one wishes to exploit such cells as truly analogue memories. To that end, we evaluated all prototyped devices for their multistate capacity via biasing them with 100 ns pulses ranging from 1 to 2 V, at 50 mV steps. In every programming cycle, a new state is assumed to have been reached if two conditions are met. First, the resistive state is sufficiently stable over time, as evaluated by retention testing. Second, the lower bound of the standard deviation of a series of $50 \times 0.5V$ read pulses is at least 2σ higher than the upper bound of the previous state (see Methods and supplementary figures S3–S5 for more detail). Using this evaluation routine, we observed a significant increase in the number of attainable resistive states for the bilayer devices in contrast to the single-layer cells. While in the case of TiO_2-only devices a maximum of 10 states on average was identified, the introduction of a barrier layer resulted into both increasing the number of resistive states significantly but also improving the dynamic response of the devices. Figure 2 summarises the switching performance of all developed bilayer ReRAM cells both in terms of the number of attainable memory states and the resistive state dynamic range. All device prototypes that encompass an active bi-layer show improvements in both performance metrics.

The performance of the Al_xO_y/TiO_2 devices is exemplified in figure 3a where a record number of 92 states is reported, which corresponds to a single cell with 6.5 bits memory capacity. This cumulative probability distribution function graph clearly illustrates the overall discernibility of the resistive states. Retention characteristics of a selection of states of a typical Al_xO_y/TiO_2 device are shown in figure 3c and 3d over a period of 8 hours at room temperature and at 85°C. It can be observed that the stored memory states are stable and remain clearly distinguishable even in the 30–40 kΩ range where the states are closely packed.

The Al_xO_y/TiO_2 combination proved to yield the best analogue performance given the "state expanse" figure of merit: ($\max\{R/R_o\} \times$ (# of states), where R_o is the baseline resistance. The improved stability allows us the programming of such elements in an arbitrary manner, as shown in figure 4. More

specifically, single 100 ns wide pulses at 2 V allow us to sequentially set the resistive state of the device gradually. Selection of a different memory state can be done by first "flushing" the device back to its baseline resistance (27.5 kΩ) via a train of 100 ns wide RESET pulses at −2 V and then applying a corresponding number of SET pulses to reach the desired memory state. The resistive state of the device can also be selected by modulating not only the number of pulses but the duration or the amplitude of the programming pulse. As figure 4 shows by modifying the duration of the pulse or the amplitude similar high resistive state to the sequential pulsing can be exhibited clearly illustrating the time-voltage dilemma. However the resolution of the device suffers as several resistance levels are suppressed. It is apparent that using smaller, more incremental and precise pulsing steps makes extracting more usable resistive states from the memory cell possible.

The remarkable analogue memory performance and stability of states can be attributed to the specific ratio of the ionic transference numbers of the second oxide layer. By observation of the data shown in Figure 2, a clear trend can be identified for the number of available states, whereas no particular trend on particular dependence can be observed. The highest number of stable non-volatile resistive states is achieved with the introduction of Al_2O_3, followed by Ta_2O_5, WO_3, HfO_2, ZnO and SiO_2. It has been recently shown that many oxide thin films used for ReRAMs have mobile host cations[29] and that as expected the oxidation state and stoichiometry of the matrix is also playing a significant role[40]. Mobility of cations and anions during high field oxide formation on metals using liquid electrolytes is well known from classical electrochemistry. In high voltages and low film thickness conditions, the transport is field-accelerated and the particular ionic transference numbers depend on the field. Al_2O_3 is identified as having the highest cation transference number, followed by Ta_2O_5, WO_3 and HfO_2[41–43]. The identified trend in the data of Figure 2 strictly correlates with the higher mobility of cations or lower mobility of oxygen ions, respectively. Similar effect of the oxygen mobility on the device stability has been reported for STO using barrier layers of Al_2O_3 (low O^{2-} mobility) and yttria-stabilized ZrO_2 (high O^{2-} mobility)[44]. We can therefore conclude that the main factor influencing the observed device performance is attributed to the transport properties of the interfacial film added to the TiO_2 layer.

It is important to mention that our characterisation routine foregoes the use of compliance current limiting, while toggling between resistive states. Current compliance limiting is a common practice that is used to control the size of the conductive filament and consequently the overall resistance of the device[45,46]. Instead, we have opted for a more direct approach by sequentially pulsing the device until its state stabilises. As the energy budget is increased incrementally until the resistance exceeds a predefined tolerance, we ensure that the minimum amount of required switching energy is expended. Figure 3b depicts the calculated programming energy requirements of a typical Al_xO_y/TiO_2 device with 47 distinct states. An upper bound of the energy consumption per state during programming can be estimated as $\sum\{V^2 /R_{min,max}\Delta t\}$, where V is the programming pulse voltage amplitude and Δt the pulse width. As biasing typically occurs between 1 and 2 V, $R_{min,max}$ represent the resistance in these two voltages as calculated from the I–V characteristic in the low resistive state (see also Figure S8). For all the states of the Al_xO_y/TiO_2 device the switching energy remains in the pJ–nJ range. Even though the overall OFF/ON ratio of the devices among the resistive states is small in comparison to previous publications[47,48] the incremental biasing steps used in this paper allow for further exploitation of the resistive values of the device that would otherwise not be possible with larger ratios. In addition our approach alleviates issues of poor retention performance mentioned in these works[47,48].

As far as the statistical distribution of the resistive states for different bilayers is concerned we can observe in figure 5a that Al_xO_y/TiO_2 bilayer clearly outperforms the other combinations with a median of 47 states (5.5 bits), followed by WO_x/TiO_2 and Ta_xO_y/TiO_2 with a median in the 4-bit range and finally by ZnO_x/TiO_2 and SiO_x/TiO_2 in the 3-bit range. Even in the worst case the Al_xO_y/TiO_2 devices

consistently exhibit at least 4-bit of information with half of the devices surpassing 5-bits and 1/3 the 6-bit mark (figure 5b).

In this paper, we demonstrated that the incorporation of different metal-oxide barrier layers in ReRAM improves the overall programming stability. This is enabled via the improved transport properties of the device depending on the increasingly higher mobility of cations and subsequent lower mobility of oxygen ions, in accordance to the employed barrier layer. Through this study, we were able to demonstrate for the first-time solid-state ReRAM operating as analogue memory cells with up to 5.5-bits capacity. While ReRAM technologies have been mainly promoted for high-spatial density storage and corollary applications, our work demonstrates the new prospects arising from high-capacity memory.

Methods

Device fabrication: All devices have been fabricated on 6-inch oxidised silicon wafers (200 nm of thermal SiO_2). Initially the bottom electrodes were fabricated using photolithography and electron beam evaporation of titanium (5 nm) and platinum (10 nm) followed by lift-off process in N-Methyl-2-pyrrolidone (NMP). Then, 40 nm of TiO_2 were deposited using magnetron sputtering. The Al_2O_3, Ta_2O_5, and SiO_2 layers (4 nm) were also deposited using magnetron sputtering after negative tone photolithography. The active layer is formed after lift-off in NMP. The 4 nm layers of ZnO, HfO_2 and WO_3 were synthesised using atomic layer deposition (ALD). After that a positive tone photolithography and ion beam milling processes were used to pattern and etch the active layers. The top electrode was fabricated using photolithography, electron beam evaporation of platinum (10 nm) and lift-off in NMP.

Electrical characterisation: Characterisation of the memristors has been done with our in-house memristor characterisation platform[49]. All read pulses are set at 50 ms in duration and 0.5 V in amplitude. Nominal line resistance for all devices evaluated is estimated to be about 150 Ω per platinum electrode. Devices are initially electroformed to a usable resistance range (25 to 200 kΩ, depending on the stack) using consecutive 1 µs pulses of negative polarity ranging from -8 to -12 V in amplitude. A series resistor of 1 kΩ was used as a current-limiting mechanism for all devices. Resistance initially drops to the 10^6 Ω range and then to a more stable 10^4–10^5 Ω range. Multi-bit capability of the devices has been evaluated with a custom algorithm (see following section). In order to extract the retention curve a sequence of 100 ns 2 V pulses is used to program the device to a specified resistance and then a read pulse is applied every 5 minutes for 8 hours. For temperature dependent retention measurements resistive level was selected after 85°C have been stabilised in the probe station chuck.

Resistive state evaluation algorithm: State assessment occurs over three phases. During the first phase a series of programming pulses of a predefined duration (100 ns), increasing amplitudes and alternating polarities is applied to the device under test and the resistive state of the device is evaluated between every pair of programming trains. This is to determine the polarity that induces a switch in the resistance of the device. After the switching polarity has been determined the second phase, using fixed amplitude, 100 ns pulses of the opposite polarity in respect to the one determined in the first phase, drives the resistance to a stable low value. Stability is assumed when the fitted slope is lower that a predefined threshold. The third phase applies an increasing number of 100 ns programming pulsing using the polarity determined from the first phase followed by two read trains separated by a 100 ms retention interval. If the lower bound of the standard deviation of the resistance measured between these trains is at least 2σ higher than the upper bound of the previous state a new resistive state is established. The algorithm terminates if the voltage limit is reached or if the trend of the resistive states become non-monotonic. The granularity on the standard deviation directly impacts the number of assessed states (see supplementary figure S3). 2σ was used throughout the electrical characterisation as it provides a

large enough confidence interval (at least 95%) while allowing the exploitation of a high amount of resistive states. A flowchart detailing the steps of the algorithm described here can be found in supplementary Fig. S4.

Data Availability: The data that support the findings of this study are available from the corresponding author upon request, as detailed in http://www.nature.com/authors/policies/data/data-availablity-statements-data-citations.pdf.

References

1. Chua, L. Memristor-The missing circuit element. *IEEE Transactions on Circuit Theory* **18,** 507–519 (1971).
2. Yoshida, C., Tsunoda, K., Noshiro, H. & Sugiyama, Y. High speed resistive switching in Pt/TiO2/TiN film for nonvolatile memory application. *Appl. Phys. Lett.* **91,** 223510 (2007).
3. Prezioso, M. *et al.* Training and operation of an integrated neuromorphic network based on metal-oxide memristors. *Nature* **521,** 61–64 (2015).
4. Serb, A. *et al.* Unsupervised learning in probabilistic neural networks with multi-state metal-oxide memristive synapses. *Nature Communications* **7,** ncomms12611 (2016).
5. Borghetti, J. *et al.* 'Memristive' switches enable 'stateful' logic operations via material implication. *Nature* **464,** 873–876 (2010).
6. Yang, J. J., Strukov, D. B. & Stewart, D. R. Memristive devices for computing. *Nat Nano* **8,** 13–24 (2013).
7. Meijer, G. I. Who Wins the Nonvolatile Memory Race? *Science* **319,** 1625–1626 (2008).
8. Tyson, S., Wicker, G., Lowrey, T., Hudgens, S. & Hunt, K. Nonvolatile, high density, high performance phase-change memory. in *2000 IEEE Aerospace Conference. Proceedings (Cat. No.00TH8484)* **5,** 385–390 vol.5 (2000).
9. Scott, J. F. & Araujo, C. A. P. de. Ferroelectric Memories. *Science* **246,** 1400–1405 (1989).
10. Waser, R. & Aono, M. Nanoionics-based resistive switching memories. *Nat Mater* **6,** 833–840 (2007).
11. Setter, N. *et al.* Ferroelectric thin films: Review of materials, properties, and applications. *Journal of Applied Physics* **100,** 051606 (2006).
12. Hamann, H. F., O'Boyle, M., Martin, Y. C., Rooks, M. & Wickramasinghe, H. K. Ultra-high-density phase-change storage and memory. *Nat Mater* **5,** 383–387 (2006).
13. Strachan, J. P., Torrezan, A. C., Medeiros-Ribeiro, G. & Williams, R. S. Measuring the switching dynamics and energy efficiency of tantalum oxide memristors. *Nanotechnology* **22,** 505402 (2011).
14. Pi, S., Lin, P. & Xia, Q. Cross point arrays of 8 nm × 8 nm memristive devices fabricated with nanoimprint lithography. *Journal of Vacuum Science & Technology B, Nanotechnology and Microelectronics: Materials, Processing, Measurement, and Phenomena* **31,** 06FA02 (2013).
15. Khiat, A., Ayliffe, P. & Prodromakis, T. High Density Crossbar Arrays with Sub- 15 nm Single Cells via Liftoff Process Only. *Scientific Reports* **6,** srep32614 (2016).
16. Baek, I. G. *et al.* Highly scalable nonvolatile resistive memory using simple binary oxide driven by asymmetric unipolar voltage pulses. in *IEDM Technical Digest. IEEE International Electron Devices Meeting, 2004.* 587–590 (2004). doi:10.1109/IEDM.2004.1419228
17. Merced-Grafals, E. J., Dávila, N., Ge, N., Williams, R. S. & Strachan, J. P. Repeatable, accurate, and high speed multi-level programming of memristor 1T1R arrays for power efficient analog computing applications. *Nanotechnology* **27,** 365202 (2016).
18. Prakash, A., Deleruyelle, D., Song, J., Bocquet, M. & Hwang, H. Resistance controllability and variability improvement in a TaOx-based resistive memory for multilevel storage application. *Appl. Phys. Lett.* **106,** 233104 (2015).
19. Zhao, L. *et al.* Multi-level control of conductive nano-filament evolution in HfO2 ReRAM by pulse-train operations. *Nanoscale* **6,** 5698–5702 (2014).

20. Lee, S. R. *et al.* Multi-level switching of triple-layered TaOx RRAM with excellent reliability for storage class memory. in *2012 Symposium on VLSI Technology (VLSIT)* 71–72 (2012). doi:10.1109/VLSIT.2012.6242466

21. Park, J. *et al.* Multibit Operation of TiOx-based ReRAM by Schottky Barrier Height Engineering. *IEEE Electron Device Letters* **32,** 476–478 (2011).

22. Kim, W. *et al.* Multistate Memristive Tantalum Oxide Devices for Ternary Arithmetic. *Scientific Reports* **6,** srep36652 (2016).

23. Wong, H. S. P. *et al.* Metal–Oxide RRAM. *Proceedings of the IEEE* **100,** 1951–1970 (2012).

24. Lee, M.-J. *et al.* A fast, high-endurance and scalable non-volatile memory device made from asymmetric Ta2O5−x/TaO2−x bilayer structures. *Nat Mater* **10,** 625–630 (2011).

25. Torrezan, A. C., Strachan, J. P., Medeiros-Ribeiro, G. & Williams, R. S. Sub-nanosecond switching of a tantalum oxide memristor. *Nanotechnology* **22,** 485203 (2011).

26. Murdoch, B. J. *et al.* Memristor and selector devices fabricated from HfO 2−x N x. *Applied Physics Letters* **108,** 143504 (2016).

27. Strukov, D. B., Snider, G. S., Stewart, D. R. & Williams, R. S. The missing memristor found. *Nature* **453,** 80–83 (2008).

28. Yang, J. J. *et al.* Memristive switching mechanism for metal/oxide/metal nanodevices. *Nat Nano* **3,** 429–433 (2008).

29. Wedig, A. *et al.* Nanoscale cation motion in TaOx, HfOx and TiOx memristive systems. *Nat Nano* **11,** 67–74 (2016).

30. Kwon, D.-H. *et al.* Atomic structure of conducting nanofilaments in TiO2 resistive switching memory. *Nat Nano* **5,** 148–153 (2010).

31. Cho, D.-Y., Luebben, M., Wiefels, S., Lee, K.-S. & Valov, I. Interfacial Metal–Oxide Interactions in Resistive Switching Memories. *Applied Materials and Interfaces* **9,** 19287–19295 (2017).

32. Alekseeva, L., Nabatame, T., Chikyow, T. & Petrov, A. Resistive switching characteristics in memristors with Al2O3/TiO2 and TiO2/Al2O3 bilayers. *Jpn. J. Appl. Phys.* **55,** 08PB02 (2016).

33. Improvement of resistive switching performances via an amorphous ZrO2 layer formation in TiO2-based forming-free resistive random access memory. *Journal of Applied Physics* **116,** 124514 (2014).

34. Yu, S., Wu, Y., Chai, Y., Provine, J. & Wong, H. S. P. Characterization of switching parameters and multilevel capability in HfOx/AlOx bi-layer RRAM devices. in *Proceedings of 2011 International Symposium on VLSI Technology, Systems and Applications* 1–2 (2011). doi:10.1109/VTSA.2011.5872251

35. Hudec, B. *et al.* Resistive switching in TiO2-based metal–insulator–metal structures with Al2O3 barrier layer at the metal/dielectric interface. *Thin Solid Films* **563,** 10–14 (2014).

36. Yoon, J. H. *et al.* Current Limit and Self-Rectification Functionalities in the TiO2/HfO2 Resistive Switching Material System. *Nanoscale* (2017). doi:10.1039/C7NR02215H

37. Valov, I. Interfacial interactions and their impact on redox-based resistive switching memories (ReRAMs). *Semicond. Sci. Technol.* **32,** 093006 (2017).

38. Carta, D. *et al.* Investigation of the Switching Mechanism in TiO2-Based RRAM: A Two-Dimensional EDX Approach. *ACS Appl. Mater. Interfaces* **8,** 19605–19611 (2016).

39. Carta, D. *et al.* X-ray spectromicroscopy investigation of soft and hard breakdown in RRAM devices. *Nanotechnology* **27,** 345705 (2016).

40. Moors, M. *et al.* Resistive Switching Mechanisms on TaOx and SrRuO3 Thin-Film Surfaces Probed by Scanning Tunneling Microscopy. *ACS Nano* **10,** 1481–1492 (2016).

41. Davies, J. A., Domeij, B., Pringle, J. P. S. & Brown, F. The Migration of Metal and Oxygen during Anodic Film Formation. *J. Electrochem. Soc.* **112,** 675–680 (1965).

42. Brown, F. & Mackintosh, W. D. The Use of Rutherford Backscattering to Study the Behavior of Ion-Implanted Atoms During Anodic Oxidation of Aluminum: Ar, Kr, Xe, K, Rb, Cs, Cl, Br, and I. *J. Electrochem. Soc.* **120,** 1096–1102 (1973).

43. Verkerk, B., Winkel, P. & de Groot, D. G. On the mechanism of anodic oxidation of Tantalum. *Philips Res. Repts* **13,** 506–508 (1958).

44. Whitton, J. L. The Measurement of Ionic Mobilities in the Anodic Oxides of Tantalum and Zirconium by a Precision Sectioning Technique. *J. Electrochem. Soc.* **115,** 58–61 (1968).

45. Baeumer, C. *et al.* Spectromicroscopic insights for rational design of redox-based memristive devices. *Nature Communications* **6,** ncomms9610 (2015).
46. Jo, S. H. & Lu, W. CMOS Compatible Nanoscale Nonvolatile Resistance Switching Memory. *Nano Lett.* **8,** 392–397 (2008).
47. Wang, Y.-F., Lin, Y.-C., Wang, I.-T., Lin, T.-P. & Hou, T.-H. Characterization and Modeling of Nonfilamentary $Ta/TaO_x/TiO_2/Ti$ Analog Synaptic Device. *Scientific Reports* **5,** srep10150 (2015).
48. Govoreanu, B. *et al.* Vacancy-modulated conductive oxide resistive RAM (VMCO-RRAM): An area-scalable switching current, self-compliant, highly nonlinear and wide on/off-window resistive switching cell. in *2013 IEEE International Electron Devices Meeting* 10.2.1-10.2.4 (2013). doi:10.1109/IEDM.2013.6724599
49. Berdan, R. *et al.* A -Controller-Based System for Interfacing Selectorless RRAM Crossbar Arrays. *IEEE Transactions on Electron Devices* **62,** 2190–2196 (2015).

Figure captions

Fig. 1: Comparison between TiO_2-only devices and Al_xO_y/TiO_2 bilayer devices (**a**) SEM micrograph of a memristor device; (**b**) Schematic representation of a single layer TiO_2-based device with platinum top and bottom electrodes; (**c**) Schematic representation of a bilayer Al_xO_y/TiO_2-based device with platinum top and bottom electrodes; (**d**) Typical bipolar switching of a device based on the stack pictured in (b) using 100 ns pulses of alternating polarity voltage ramps ranging from 1 to 2 V, with voltage steps of 200 mV; (**e**) Typical bipolar switching of a device based on the stack pictured in (c) using 100 ns pulses of alternating polarity voltage ramps ranging from 1 to 2 V with voltage steps of 200 mV. The coloured horizontal lines in fig. (d) and (e) denote the average low (LRS) and high resistive state (HRS).

Fig. 2: Multibit evaluation of devices based on different barrier layer combinations. Number of attainable resistive states (left axis) and ratio of the final state resistance over the baseline resistance (right axis) for typical bilayer devices. Confidence interval for the state assessment is 2σ following the routine described in supplementary Fig. S4 and S5. A chart containing each individual state assessed for every bilayer combination can be found in supplementary figs. S6 and S7.

Fig. 3: Multibit operation of a device using the Al_xO_y/TiO_2 RRAM stack. (**a**) Cumulative probability distribution function plot of a device with a record of 92 distinct resistive states. All states are read at 0.5 V are closely packed and individually discernible; (**b**) switching energy required to switch a typical Al_xO_y/TiO_2 device. Only the energy expended during programming is regarded for this graph; (**c**) 8 hours retention measurements for select resistive states at room temperature. (**d**) 8 hours retention

measurements for select resistive states at 85°C. Resistance can be retained even at elevated temperatures.

Fig. 4: Programming the Al_xO_y/TiO_2 device. Modes of selecting specific resistive states. Starting from a baseline resistance of ~27.5 kΩ a specific resistive state can be attained with different modes of programming, by modulating **(i)** the number of pulses, **(ii)** the duration of the pulses or **(iii)** the amplitude of the pulse. Using multiple pulses of lower amplitude and pulse width can help in pinpointing resistive states that otherwise could not have been discerned. In between the state selection the device is flushed with a series of 20 RESET pulses of 100 ns in duration.

Fig. 5: Bilayer device statistics. (**a**) Number of resistive states ranges for different bilayer combinations. Al_xO_y/TiO_2 devices clearly outperform all other combinations with ZnO_x/TiO_2 and SiO_x/TiO_2 exhibiting the lower amount of resistive states; (**b**) Attainable states distribution for 32 Al_xO_y/TiO_2 based devices. Nearly all the devices tested exhibit at least 4 bits of information whereas 1/3 of them surpasses the 6-bit mark.
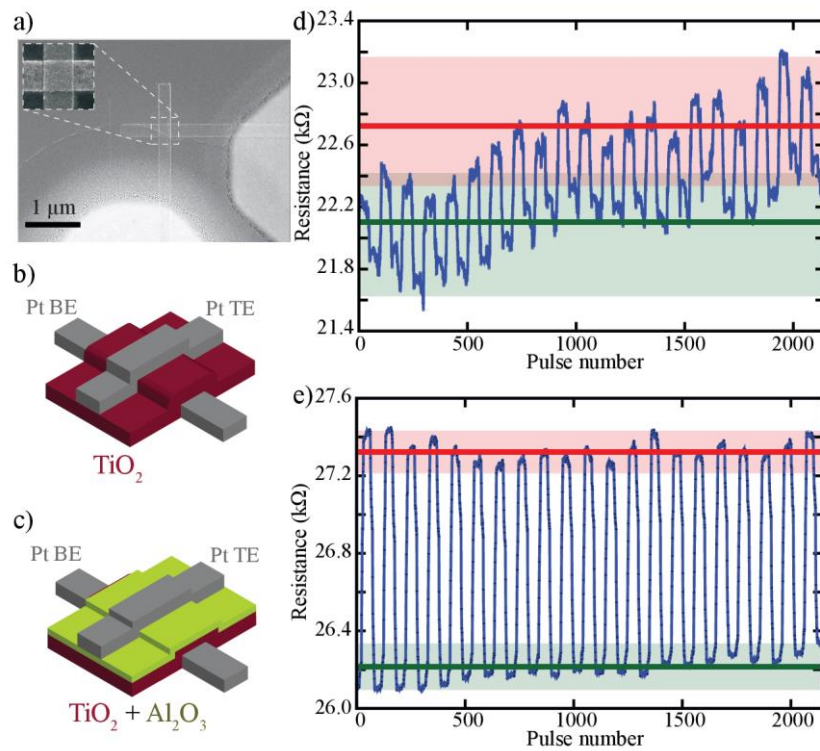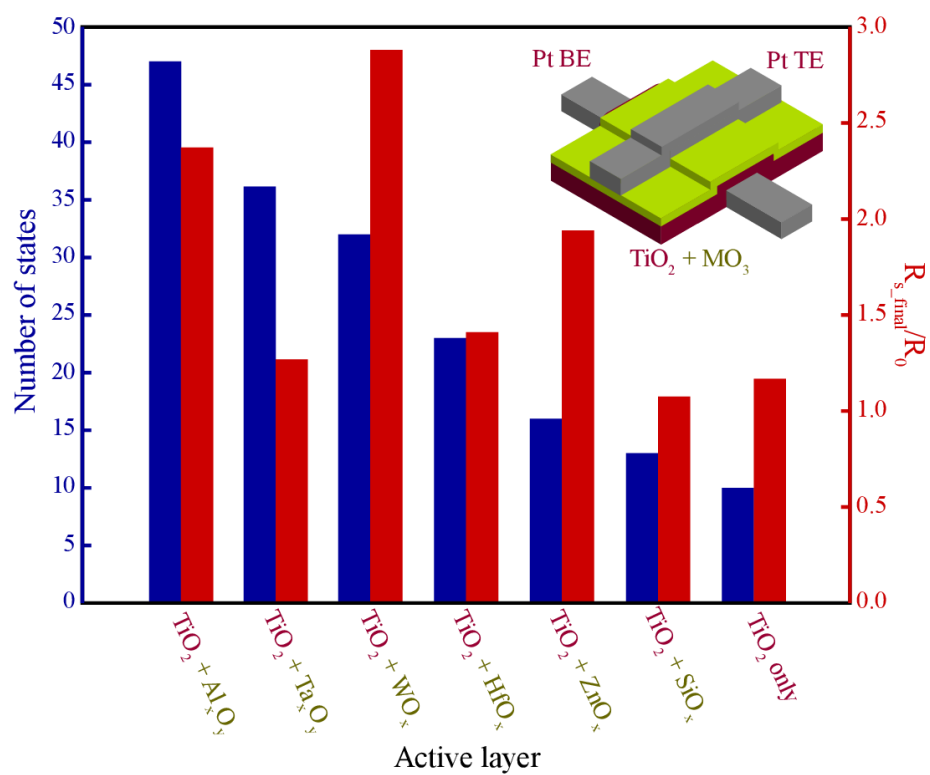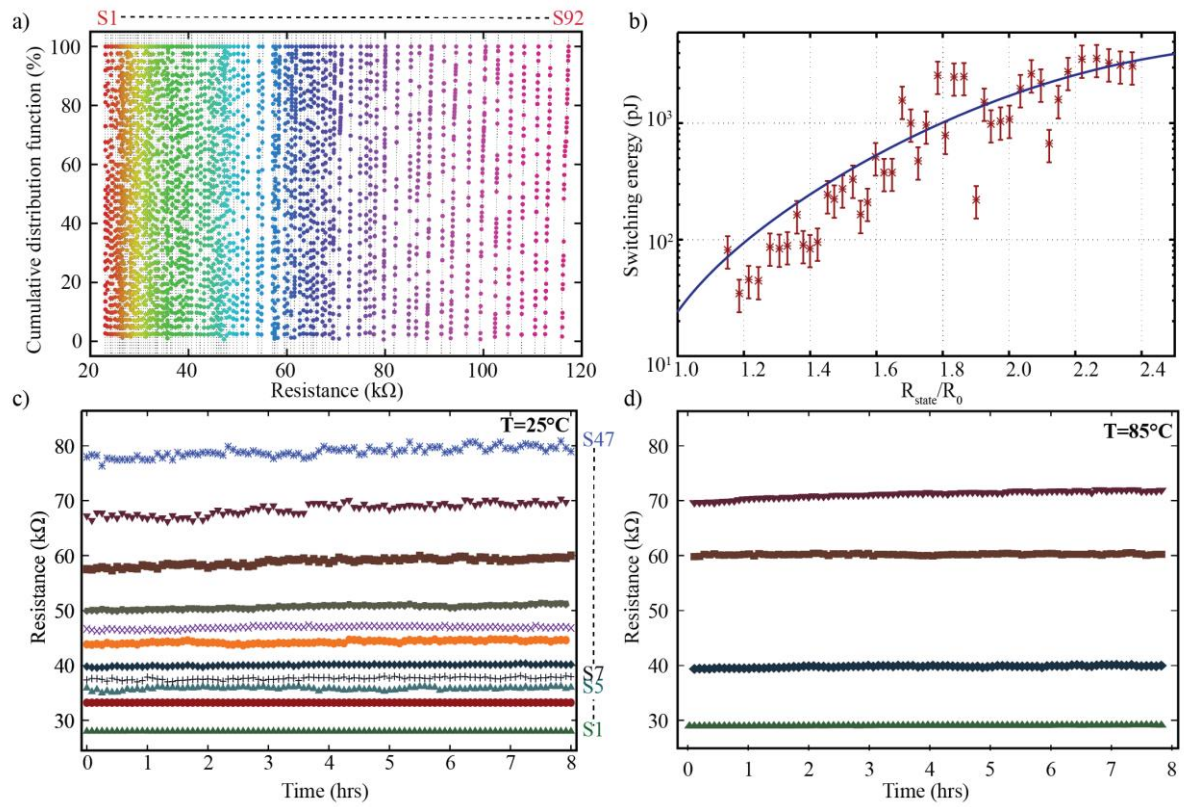
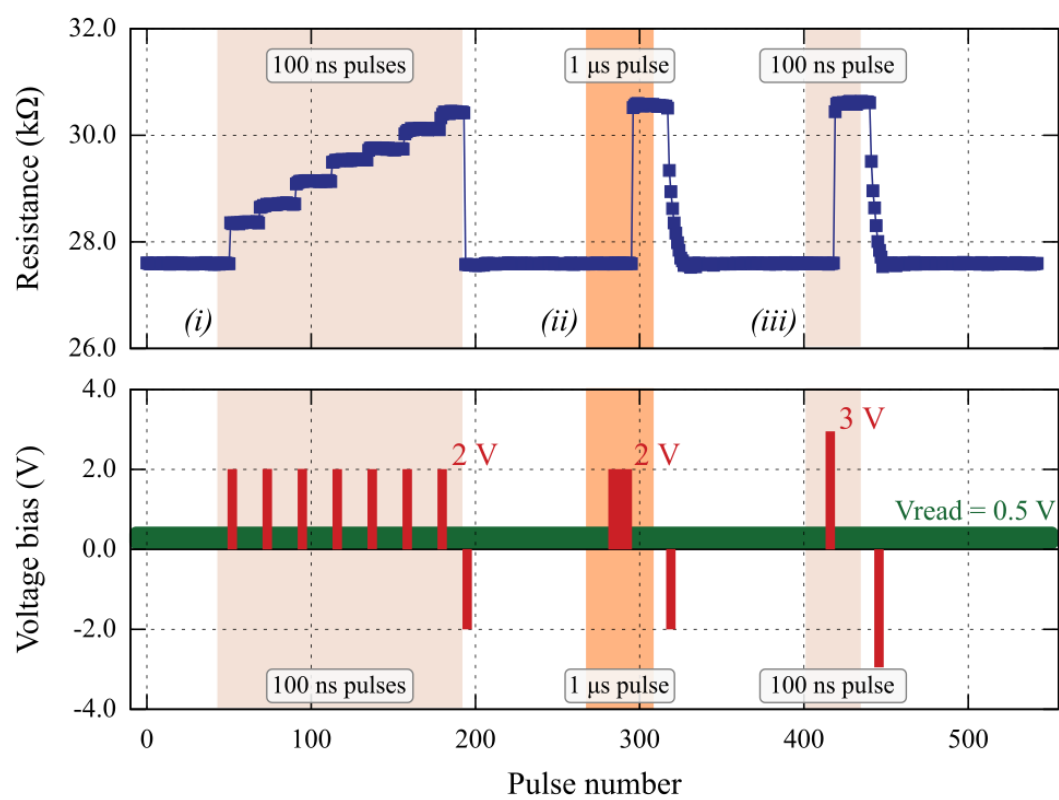**Figure 1**

Figure 2

Figure 3

Figure 4

Figure 5